# Impact of the Morphology of $V_2O_5$ Electrodes on the Electrochemical $Na^+$-Ion Intercalation

**Huinan Si,[1,2,=] Lukas Seidl,[2,3,4,5,=,*] Eileen Miao Ling Chu,[5] Slađana Martens,[2,4,5] Jiwei Ma,[2,4,5] Xinping Qiu,[1,2] Ulrich Stimming,[2,3,4,5,6] and Oliver Schneider[2,4,5,**,z]**

[1] *Department of Chemistry, Tsinghua University, 100084 Beijing, People's Republic of China*
[2] *Joint Research Institute for Advanced Power Sources for Electric Vehicles, Technische Universität München, 85748 Garching, Germany, Tsinghua University, 100084 Beijing, People's Republic of China*
[3] *Physik-Department, Technische Universität München, 85748 Garching, Germany*
[4] *Institut für Informatik VI, Technische Universität München, 85748 Garching, Germany*
[5] *Electrochemical Research Group, Technische Universität München, 85748 Garching, Germany*
[6] *Chemistry - School of Natural and Environmental Sciences, Newcastle University, Newcastle Upon Tyne NE1 7RU, United Kingdom*

The development of high performance electrodes for Na-ion batteries requires a fundamental understanding of the electrode electrochemistry. In this work, the effect of the morphology of vanadium oxide on battery performance is investigated. First, the phase transitions upon sodiation/de-sodiation of $Na_xV_2O_5$ cathodes in standard battery solvents are explored by cyclic voltammetry and X-Ray diffraction. At potentials 1.5 V positive of Na/$Na^+$ the insertion of the first $Na^+$ into pristine $V_2O_5$ is completed and α'-$NaV_2O_5$ is formed. A discharge to 1.0 V results in the introduction of a second $Na^+$ and after a deep discharge to 0 V a third $Na^+$ is intercalated. When cycled as an intercalation electrode, the Na-content $x$ in $Na_xV_2O_5$ varies between $x = 1$ (charged) and $x = 2$ (discharged). For studying the effect of electrode morphology on the battery performance, several types of $V_2O_5$ (hollow $V_2O_5$ microspheres, $V_2O_5$ nanobundles and $V_2O_5$ nanobundles blended with 10%$_{wt}$ $TiO_2$) were prepared and compared to a commercially available $V_2O_5$-micropowder. The nanobundles were prepared by a facile sonochemical process. In comparison to the microsized $V_2O_5$ morphologies, the potential plateaus in the charge/discharge curves of the $V_2O_5$ nanobundles are at more positive potentials and the capacity loss in the first cycle is suppressed. The $V_2O_5$ nanobundles showed the best battery performance with a reversible capacity of 209.2 mAh $g^{-1}$ and an energy density of 571.2 mWh $kg^{-1}$ (2$^{nd}$ cycle). After an initial capacity fading, which can be slightly suppressed by blending the $V_2O_5$ with $TiO_2$, the pure $V_2O_5$ nanobundles have a practical capacity of 85 mAh $g^{-1}$, an operation potential of 2.4 V, an energy density of 266.5 mWh $kg^{-1}$ and a capacity retention of 83% after 100 cycles. The best battery performance of the nanomaterial is ascribed in this study to the amorphous character of the electrode, favoring faster electrode kinetics due to a (pseudo-) capacity dominated charging/discharging, reducing diffusion lengths and preventing further amorphization, which all is beneficial in terms of lifetime, capacity, operation voltage, energy density and energy efficiency.
 [DOI: 10.1149/2.0621811jes]

Manuscript submitted June 6, 2018; revised manuscript received August 8, 2018. Published August 23, 2018.

Due to daily and seasonal fluctuations, renewable energy sources, such as solar- and wind-power, require large scale energy storage devices to balance those irregularities.[1–6] Li-ion batteries (LIBs), representing the state of the art battery technology, might contribute within power-to-grid scenarios and second life application of spent electric vehicle batteries, but are no viable option for large scale energy storage, since they require the usage of the costly Li. Na-ion batteries (NIBs) are much better in that regard, because Na is one of the most abundant elements and equally distributed in the earth's crust. It is thus available in an 'unlimited' amount bringing about advantages in terms of raw material cost.[1–5,7–9]

Besides the different prices of the raw metals themselves, Li and Na also show different alloying behavior with the anode current collectors. Li forms binary Li-Al alloys at low operation potentials, which prevents the use of the low price and low weight Al current collectors at the anode. In LIBs, Cu current collectors have to be used instead. Na does not show this alloying behavior with Al, which may contribute to lower costs of NIBs compared to LIBs. Apart from the cost benefit, the lower weight of Al current collectors is also favorable for gravimetric cell energy and power density.[3,5,6]

The higher molar weight of the Na atom (23.00 g $mol^{-1}$) compared to the Li atom (6.94 g $mol^{-1}$), on the other hand, implies an intrinsic decrease of gravimetric energy- and power-density of NIBs compared to LIBs.[5] Moreover, NIBs loose energy and power density due to the more positive standard potential of $Na^+ + e^- \rightleftharpoons Na$ (−2.71 V vs SHE) in comparison to $Li^+ + e^- \rightleftharpoons Li$ (−3.04 V vs SHE).[5] Additionally, the ionic radius of the bare Na-ion with 1.02 Å is considerably larger than the ionic radius of the Li-ion with 0.76 Å.[5]

Especially the effect of the larger ionic radius of the Na-ion on its intercalation behavior is often discussed in literature. In this respect, three consequences are usually considered, the effect on the ion mobility and diffusion in the active material crystallites, the influence on battery lifetime due to larger volume expansions upon Na-ion intercalation/de-intercalation, and the formation of new crystal phases upon sodiation compared to lithiation: Often the larger ionic size is believed to hamper Na-ion diffusion compared to Li-ions. Facilitating Na-ion diffusion would therefore require a more open lattice framework of the electrode materials, providing wider diffusion channels for the larger ions.[10,11] On the other hand, the simple correlation of ionic radius and sluggish Na-ion diffusion is disputed by several studies, which deny this relationship,[12] or even claim an enhancement in Na-ion diffusion upon intercalation, since the diffusion channels expand more upon sodiation than upon lithiation.[8,13] Elsewhere,[9,11,14] it is reported that the insertion of the larger Na-ions results in a larger volume expansion of the electrode lattice, which negatively affects the battery lifetime. Additionally, the bigger ion size prevents the formation of many crystallographic phases, which are typically found in analogue Li-structures, making these materials unsuitable for NIBs, thus reducing the amount of possible electrode materials.[15] At the same time, Na can form new crystallographic phases with other host materials, which require the larger ion size and cannot be observed for Li.[8]

One material, which can equally host Li- as well as Na-ions is the layered orthorhombic transition metal oxide $V_2O_5$. $V_2O_5$ was studied excessively in LIBs, because it offers reasonable capacities[16] and can be versatilely structured, ranging from solid microspheres[17] to hollow microspheres,[18] yolk-shell microstructures,[19] microflowers,[20]

[=] These authors contributed equally to this work.
[*] Electrochemical Society Student Member.
[**] Electrochemical Society Member.
[z] E-mail: oliver_m.schneider@tum.de

sponge like microstructures[21] and several nanostructures like aerogels/xerogels,[22] nanofibers[23] and nanoflakes.[24]

Some of these $V_2O_5$ structures have already been tested in NIBs. Nanostructured bilayered $V_2O_5$,[25] bilayered $V_2O_5$ nanobelts,[26] amorphous $V_2O_5$,[27] hierarchical orthorhombic $V_2O_5$ hollow nanospheres[10] and hydrated vanadium pentoxide ($V_2O_5 \cdot nH_2O$)[28] were used as cathodes, while a layered $V_2O_5$ aerogel[29] served as anode. A general drawback of $V_2O_5$ electrodes in LIBs and NIBs is their limited lifetime. One strategy to increase the lifetime in LIBs was to either protect the $V_2O_5$ particles by a $TiO_2$ coating,[30–32] which forms a beneficial solid electrolyte interphase and slows down the $V_2O_5$ dissolution, or to physically mix $V_2O_5$ with small amounts of $TiO_2$,[33] which prevents $V_2O_5$ dissolution by a preferential reduction of $Ti^{4+}$. The physical mixture of $TiO_2$ to $V_2O_5$ has not yet been reported for NIBs and is part of this study.

The crystal structure of the layered oxide $V_2O_5$, an orthorhombic *Pmmn* lattice,[34] not only undergoes phase transitions upon lithiation,[35] but also during sodiation.[36] There are different crystal phases of the $Na_xV_2O_5$ reported in literature. Depending on the $x$-value, the $Na_xV_2O_5$ is in its α-phase for $0 < x < 0.02$.[37] For $0.2 < x < 0.4$ the β-phase is formed,[37] while the specific composition of $Na_{0.64}V_2O_5$ is called τ-phase.[36,37] From $0.7 < x < 1$ one can find the α'-phase[36] and for higher Na contents the η-phase ($1.45 < x < 1.8$) and the κ-phase ($1.68 < x < 1.82$).[38]

The aim of this study is to investigate in depth the electrochemistry of $V_2O_5$ positive electrodes operated in a NIB, especially the role of morphology. Based on a general understanding of the $Na_xV_2O_5$-phase transitions gained from electrochemical measurements, different electrode morphologies, ranging from nano- to microstructures, are tested with respect to their operating performance in a NIB, giving an insight into the morphology influence of the electrode material on the $Na^+$-intercalation behavior. A focus lies on the performance of sonochemically prepared nanomaterial, as sonochemistry often permits the fabrication of nanomaterials under relatively mild conditions. In addition, the impact of incorporating $TiO_2$ in $V_2O_5$ is studied for the first time in NIBs. For comparison, also commercial oxide and micron-sized material prepared using a solvothermal method are studied.

## Experimental

The four different $V_2O_5$-powders used to prepare electrodes were a commercially available $V_2O_5$-powder (99.99%, Alfa Aesar Puratronic) in addition to three self-synthesized materials. Hollow layered $V_2O_5$-microspheres were solvothermally synthesized at 180°C for 24 h from a 75 mM $NH_4VO_3$ (99.0%, Eastern chemical works) in ethylene glycol (AR, Beijing chemical works) solution in a home-built Teflon autoclave and a subsequent 2 h calcination at 450°C in air, following a recipe of Uchaker et al.[39] A sonochemical route was used to prepare $V_2O_5$-nanobundles from an aqueous 50 mM $V_2O_5$ (99.99%, Alfa Aesar Puratronic) and 100 mM NaF (99.99%, Alfa Aesar) solution. During sonication, the temperature of the reactor was kept constant at 50°C (Julabo F25), while ultrasound (Bandelin Sonopuls homogenizer, Bandelin UW3200 generator, Bandelin VS70/T sonotrode, at 100% amplitude setting) was applied for 2 h.[40] The same procedure was used for the preparation of $TiO_2$-blended $V_2O_5$-nanobundles, where 10%$_{wt}$ (80 mM) of $TiO_2$ (99%, Alfa Aesar) was added to the solution. After sonication, the residual NaF was removed by washing the formed solid precipitate three times with MilliQ-water followed by centrifugation (Eppendorf Centrifuge 5810 R), before the oxide was dried in air. Powders were characterized by Scanning Electron Microscopy (SEM; Zeiss EVO MA10 and Hitachi S 5500), Energy Dispersive X-Ray Spectroscopy (EDS; Hitachi S 5500), X-Ray Diffraction (XRD, Bruker AXS D8 Advance Instruments), X-Ray Photoelectron Spectroscopy (XPS, PHI Quantera SXM and Scanning X-ray Microprobe, ULVAC-PHI). Ex-situ XRD measurements on the phase transitions and the electrode lifetime were conducted on electrodes prepared from a commercial $V_2O_5$ powder (99.2%, Alfa Aesar).

Electrodes were coated on Al-foil (15 μm, PI-KEM Ltd and Qinhuangdao Xingheng Aluminium-Tech Co.) from $V_2O_5$-slurries, containing 80%$_{wt}$ active material, 10% conductive carbon (Timical SuperC65 and SuperP) and 10% PVDF-binder (Kynar 900 HSV, and 99%, Sigma Aldrich). The powders were diluted with N-Methyl-2-pyrrolidon (NMP, 99.5%, anhydrous, Sigma Aldrich) until a 250 μm thick film could be prepared by an electrode coater (RK K Control Coater and MIT Corporation Automatic Thick Film Coater MSK-AFA-III). After drying, circular electrodes (10 mm in diameter) were punched and mechanically pressed with 1 bar pressure (Mauthe Maschinenbau, KBr-press PE-011 and Shenzhen POXON Machinery technology Co., experimental roller press PX-GY-100). Before battery assembly, the electrodes, as well as glass fiber separators (VWR collection, particle retention: 1.6 μm) were vacuum dried for 2 h at 120°C (Büchi Glass Oven B-585 and Shanghai Yiheng Instruments Company, DZF-6050).

Electrochemical tests were performed in three-electrode T-type Swagelok cells. Metallic Na (99.9%, Sigma Aldrich and 99.5%) served as reference and counter electrode, while a 1 M $NaClO_4$ (98.0%, anhydrous, Alfa Aesar) in ethylene carbonate (EC) (99%, anhydrous, Sigma Aldrich) / propylene carbonate (PC) (99.7%, anhydrous, Sigma Aldrich) (1:1) electrolyte was used. The electrodes were separated by glass fiber separators (VWR collection, 1.6 μm particle retention), which were soaked with the electrolyte. The cells were assembled in an Ar-filled glove box (MBRAUN, MB 200 B glove box, MB 20 G LMF gas) with $O_2$- and $H_2O$-contents below 1 ppm. Charge/discharge tests were measured with Gamry potentiostats (Interface 1000) with the Gamry Instruments Framework Data Acquisition Software (Version 6.10 & 6.25). Electrochemical parameters, such as current densities, specific capacities, energy densities and specific differential capacities in dQ/dV-plots are normalized to the $V_2O_5$-, respectively $V_2O_5 + TiO_2$-masses.

## Results

***Sample characterization.—***In order to study the influence of the $V_2O_5$ morphology on the battery performance, different morphologies were synthesized and characterized before use. A commercial $V_2O_5$ powder used as reference, consisting of solid micro grains with typical dimensions of 0.5 μm × 0.5 μm × 1.0 μm (*cf.* SEM micrographs in Figures 1a and 1b) shows the largest crystallinity according to XRD data (Figure SI 1). Figure SI 1 presents the baseline corrected diffractograms. The XPS analysis (Figure SI 2 and Figure SI 3) reveals the purity of this powder and serves as reference for the other samples in this study. Figure SI 3a shows a detailed analysis of the O1s, $V2p_{1/2}$ and $V2p_{3/2}$ peaks of the commercial sample.

From a solvothermal synthesis hollow layered $V_2O_5$ microspheres were synthesized. The SEM images (Figures 1c and 1d) show 3 μm to 5 μm large spheres having a hollow core, while the shell consists of solid particles with dimensions in the range of 0.1 μm × 0.1 μm × 0.1 μm. The estimated crystallinity of these particles is lower than that for the commercial $V_2O_5$ (Figure SI 1). The full XPS-spectra (Figure SI 2) show Na and S contaminations stemming from the synthesis. A detailed analysis of the O1s, the $V2p_{1/2}$ and the $V2p_{3/2}$ peaks in Figure SI 3b shows the appearance of both, fully oxidized V, i.e. $V^{5+}$, and incompletely oxidized $V^{4+}$. This is most probably due to a partial reduction by the ethylene glycol during the solvothermal treatment in the synthesis and due to an O-deficiency in the autoclave.

Besides the two micron-sized samples, a nanostructured $V_2O_5$ material was synthesized via a sonochemical route. The extreme local conditions during the collapse of cavitation bubbles (~5000 K, ~1000 bar, $> 10^{10}$ K $s^{-1}$) created by ultrasound enables a facile synthesis of nanostructured materials, which are not easily accessible by other synthetic routes.[41] In the present case, the sonochemical synthesis was applied to $V_2O_5$ as an electrode material for NIBs for the first time, resulting in the formation of 500 nm long $V_2O_5$ nanobundles with thicknesses below 20 nm (Figures 1e and 1f). From XRD (Figure SI 1) a lower crystallinity compared to the commercial and the solvothermal $V_2O_5$ is found. XPS (Figure SI 2) shows a Na and

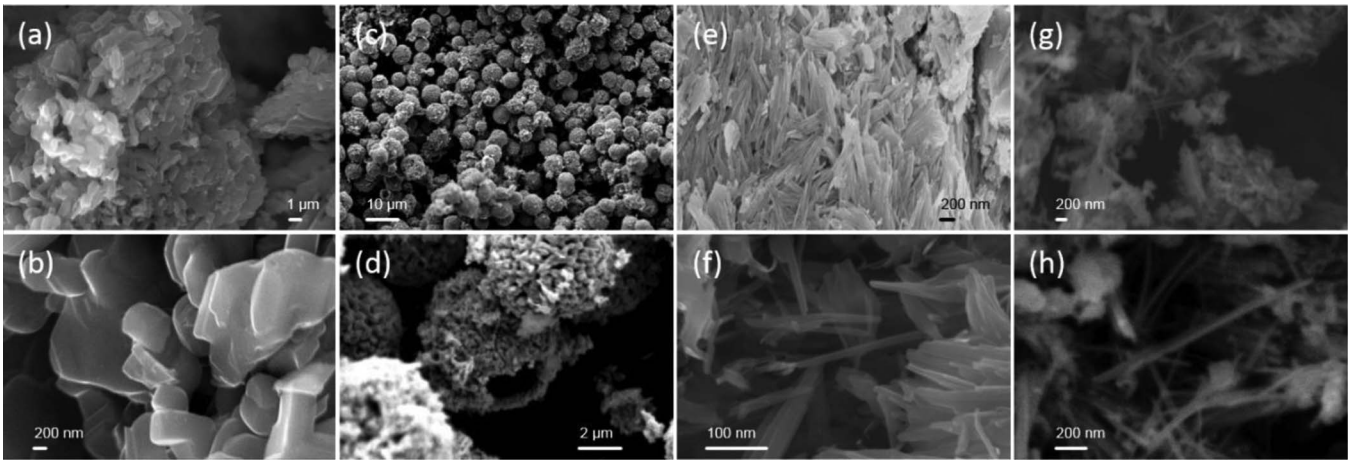


**Figure 1.** Scanning Electron Micrographs of (a, b) commercial $V_2O_5$ (Alfa Aesar Puratronic), (c, d) solvothermally synthesized $V_2O_5$ hollow layered microspheres, (e, f) ultrasonicated $V_2O_5$ nanobundles and (g, h) ultrasonicated $V_2O_5$ nanobundles blended with $10\%_{wt}$ $TiO_2$.

F contamination from the synthesis. Figure SI 3c shows the expected O1s, $V2p_{1/2}$ and $V2p_{3/2}$ peaks for a pure, fully oxidized $V_2O_5$ sample.

In order to benefit from the protective properties of physically mixing $TiO_2$ to the $V_2O_5$ and to guarantee a proper mixture on the nanoscale, sonochemistry was applied to synthesize $V_2O_5$ nanobundles blended with 10% $TiO_2$. According to the SEM images (Figures 1g and 1h) they have a similar morphology as the pure $V_2O_5$ nanobundles, i.e. ca. 1 µm long needles with a thickness of well below 50 nm. This material has the lowest crystallinity of all materials. No clear $TiO_2$ peaks are observed in the XRD diffractograms and a broad peak below 10° appears, resembling the (001) reflection of bilayered $V_2O_5$.[25,29] In the XPS signal (Figure SI 2), Ti peaks can now be found besides the still present Na and F traces. Also the O1s peak consists of a O1s($Ti^{4+}$) and a O1s($V^{5+}$) peak stemming from the titanium coordinated oxygen and vanadium coordinated oxygen, respectively. An EDS-analysis of the powder (Figure SI 4) shows that V as well as O and Ti are evenly distributed throughout the needles analyzed, confirming the homogenous physical mixture of $TiO_2$ and $V_2O_5$, even on the nanoscale. Also the fluoride is homogeneously distributed in the needles.

***Electrochemical characterization.—****Electrochemical $Na_xV_2O_5$ phase transitions.*—The cycling behavior of $V_2O_5$ in a NIB is strongly affected by the depth of discharge, which results in different phase transitions. Figure 2 shows the CVs of a $V_2O_5$ electrode cycled in a 1 M $NaClO_4$ in EC/PC solution at a potential sweep rate of 50 µV $s^{-1}$. In Figure 2a, the lower-cut off potential was limited to 1.5 V, in (b) to 1.0 V and in (c) to 0.01 V. Additionally, an ex-situ XRD measurement for each depth of discharge is shown in Figure 3, with the pristine $V_2O_5$ electrode (gray), the $V_2O_5$ electrode after a discharge to 1.5 V (red), to 1.0 V (blue) and to 0.01 V (green).

During the first discharge (negative scan, Figure 2a), a broad cathodic peak consisting of two overlapping peaks is visible arising from potentials below 2.25 V and ranging to 1.5 V. Assuming $Na^+$-intercalation, one can calculate a $Na_{0.91}V_2O_5$ stoichiometry from the discharge capacity of the thus formed $Na_xV_2O_5$ phase. This phase transition is irreversible, since no corresponding anodic peak appears upon charging the electrode. Thus, the inserted Na remains in the $Na_xV_2O_5$ lattice after the first discharge. The (001)-peak of the pristine orthorhombic $V_2O_5$ electrode with a lattice constant of 4.55 Å shifts to lower angles, as the lattice expands upon sodiation to 5.05 Å. At the same time one realizes that all other (*hkl*)-peaks with a non-zero *l*-value shift to lower angles during this phase transition, while (*hk0*)-peaks remain unaffected.

Discharging further to 1.0 V (Figure 2b), a second peak appears between 1.5 V and 1.0 V, which corresponds to a stoichiometry of $Na_{2.01}V_2O_5$. This peak now is partially reversible, i.e. the cathodic peak is accompanied by an anodic one, even though at much higher potential indicating poor kinetics. With repeated cycling, the voltammogram changes: not only the peak potentials are shifting, but also the shape of the peaks changes from sharp peaks to smeared out and broadened peaks. XRD, on the other hand (Figure 3), does not show a phase transition of the $V_2O_5$ lattice upon insertion of a second Na ion, as the peak positions do not change.

Performing a deep discharge to 0.01 V (Figure 2c), another irreversible phase transition can be observed starting below 0.75 V, which results in a disappearance of the anodic peaks and a vanishing of the XRD-peaks (Figure 3) and thus of the long-range order of the $V_2O_5$ lattice. Once the electrode is set to such low potentials ($Na_{2.6}V_2O_5$), no further phase transitions occur in the consecutive cycles.

***Battery performance.—****In order to test the battery performance, the peaks appearing in cyclic voltammetry (Figure 2) suggest cycling the $Na_xV_2O_5$ electrode in a potential range from 1.0 V to 4.0 V. Galvanostatic charge-/discharge-profiles and the dQ/dV-plots of the first three cycles for different $V_2O_5$-electrode materials cycled in 1 M $NaClO_4$ in EC/PC are shown in Figure 4. The full data set of 200 cycles can be found in Figure SI 5.

During the first discharge, the commercial $V_2O_5$ (Figure 4a) shows a total Na insertion capacity of 234.6 mAh $g^{-1}$, which decreases in the second cycle to 92.0 mAh $g^{-1}$. In consecutive cycles, the capacity continuously fades and the initially clearly visible potential plateaus lose their shape. The dQ/dV-plots of the first three cycles in Figure 4e are very similar to the CV in Figure 4b. The dQ/dV-plot also shows the cathodic twin-peak in the first discharge above 1.5 V, which causes the corresponding potential plateau during first discharge. This peak again is related to an irreversible process. The other cathodic peak above 1.0 V corresponds to the low potential plateau. As already observed in the CV (Figure 2b), this peak is accompanied by an anodic peak. Moreover, while cycling, the peaks lose intensity and shift to higher potentials.

The solvothermally synthesized hollow $V_2O_5$ microspheres have a high discharge capacity of 303.6 mAh $g^{-1}$ in the first discharge (Figure 4b). Again, since the high potential phase transition is irreversible, the capacity decreases to 129.4 mAh $g^{-1}$ in the second cycle. Interestingly, the two nanomaterials (Figures 4c and 4d) have a different behavior in this respect: here, the first cycle discharge capacity is smaller than in the second cycle.

The potential profiles and the dQ/dV-plots depict that the nanomaterials (Figures 4c, 4d, 4g and 4h) show reversible redox transitions at quite positive potentials around 2.5 V, while the highly crystalline materials (Figures 4a, 4b, 4e and 4d) mainly show phase transitions below 2 V. In comparison, the nanomaterials have less pronounced plateaus in the potential profiles.

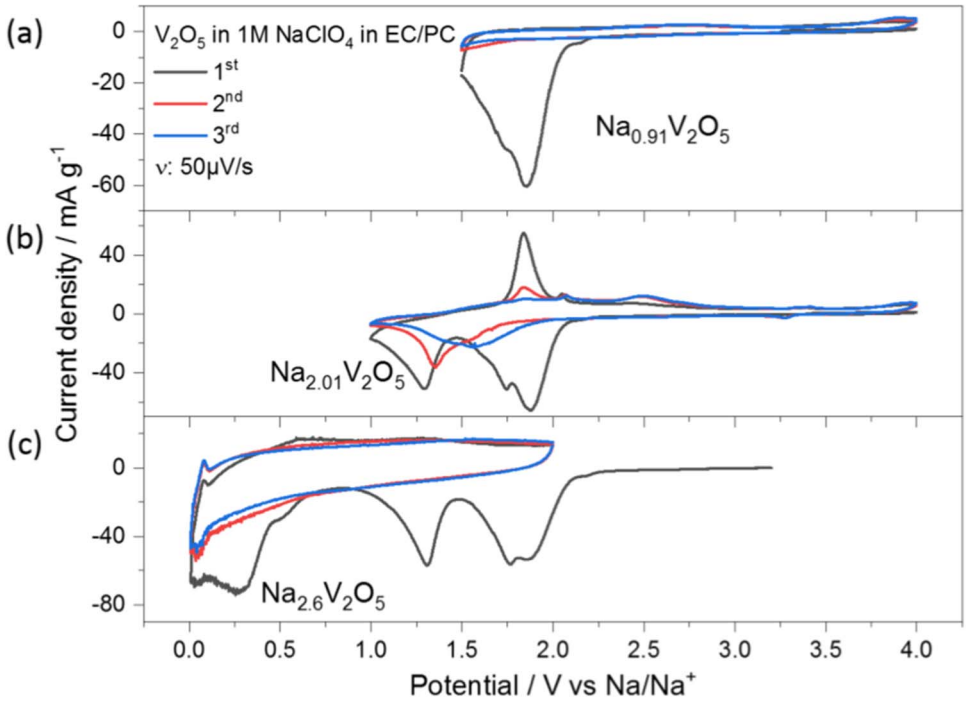


**Figure 2.** Cyclic Voltammograms of commercial $V_2O_5$ (Alfa Aesar Puratronic) in 1 M $NaClO_4$ in EC/PC (1:1) at 50 μV s$^{-1}$ showing the potential dependent phase transitions of the $Na_xV_2O_5$. (a) OCP to 4.0 V to 1.5 V, (b) OCP to 4.0 V to 1.0 V and (c) OCP to 0.01 V to 2.0 V.

Figure SI 6 displays dQ/dV-plots derived from the charge/discharge curves in Figure 4 and Figure SI 5. Figure SI 6a to 6d show dQ/dV-plots for the fifth cycle of the different materials measured at different (galvanostatic) rates, as indicated. Here, the increase of operation potential of the nanomaterials (Figure SI 6c and 6d) becomes clearly visible, since the peaks caused by the phase transitions are shifted by more than 0.5 V in comparison to the ones for the microstructures (commercial and solvothermal $V_2O_5$ (Figure SI 6a and 6b). Additionally, the rate influences the cycling behavior: the peak heights decrease with increasing rate, while the differential capacity remains unaffected by changes in charging/discharging current in the non-faradaic regime. The peaks shift in potential, which must be an effect of the rate and not just of repeated cycling, since this shift is not observed for five consecutive cycles measured at the same rate, i.e. 50 mA g$^{-1}$ as shown in Figure SI 7. The shift in peak potential is a consequence of an increase in overpotential, since the anodic peaks shift to more positive potentials, while the cathodic peaks shift to more negative potentials. A more detailed analysis of the peak shift of the marked peaks (black arrows) can be found in Figure SI 8.

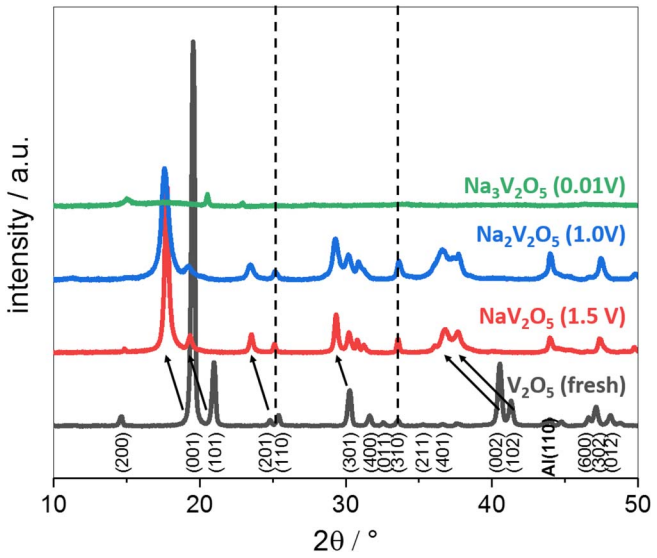


**Figure 3.** XRD patterns of the $Na_xV_2O_5$ phase transitions in dependence of the Na content $x$ (grey: fresh $V_2O_5$ electrode; red: after discharge to 1.5 V; blue: after discharge to 1.0 V; green: after discharge to 0.01 V).

The potential profiles shown in Figure 4 and Figure SI 5 are the result of a rate capability test, where the electrodes were charged/discharged at different currents. Figure 5a plots the measured charge-capacities as a function of cycle. The electrodes were cycled for five cycles each at 20 mA g$^{-1}$, 50 mA g$^{-1}$, 100 mA g$^{-1}$ and 200 mA g$^{-1}$ in the first 20 cycles, respectively.

One can observe that throughout the experiments all self-synthesized materials have a higher capacity than the commercial $V_2O_5$. This is clearly visible at low rates of 20 mA g$^{-1}$, where especially the nanomaterials show a reversible capacity of more than 200 mAh g$^{-1}$, quickly fading though. Increasing the rate to 200 mA g$^{-1}$, a capacity decrease is observed for all samples, where the sonicated $V_2O_5$ nanobundles retain the largest capacity, i.e. show the largest rate capability.

Long term cycling was performed at 50 mA g$^{-1}$. Also here the sonicated $V_2O_5$ nanobundles perform best with almost 80 mAh g$^{-1}$ capacity remaining after 200 cycles, which corresponds to an average capacity loss of 0.124 mAh g$^{-1}$ per cycle (0.12%) in the long term cycling measurement. The commercial $V_2O_5$ as well as the hollow $V_2O_5$ microspheres show a higher capacity fading, whereas the $TiO_2$ blended sample only fades at a rate of 0.061 mAh g$^{-1}$ per cycle (0.08%) and performs best in this respect.

In order to understand the degradation behavior of microgranular $V_2O_5$-electrodes in a NIB, XRD measurements of electrodes at different cycle lifetimes are presented in Figure 6. The (001)-peak intensity ($2\theta = 19.5°$), which is proportional to the crystallinity of the sample, of the uncycled $V_2O_5$-electrode (gray) decreases after one cycle (red) and shifts to lower angle ($2\theta = 17.54°$), due to the phase transition to the $NaV_2O_5$ composition. Prolonged cycling results in a disappearance of the XRD-peaks, indicating a loss of crystallinity, as can be

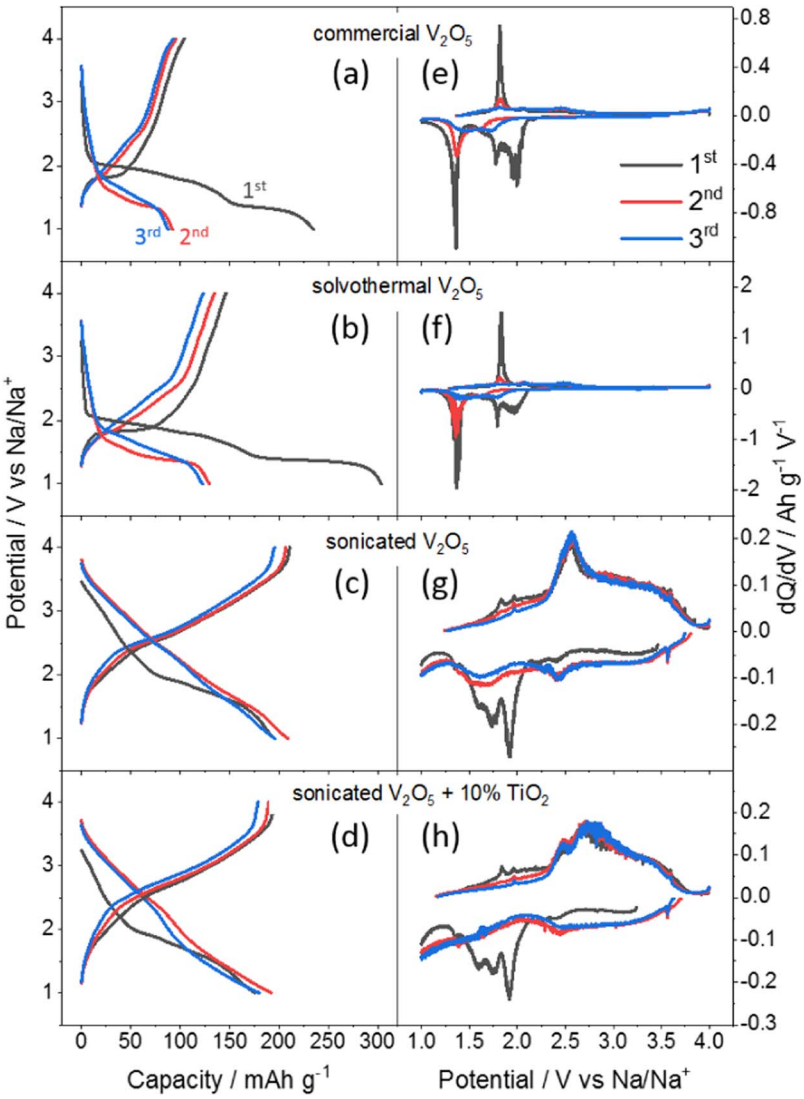


**Figure 4.** Charge-/discharge-profiles of (a) the commercial $V_2O_5$ (Alfa Aesar Puratronic), (b) the solvothermally synthesized $V_2O_5$ hollow layered microspheres, (c) the ultrasonicated $V_2O_5$ nanobundles and (d) the ultrasonicated $V_2O_5$ nanobundles blended with 10%$_{wt}$ $TiO_2$. (e) to (h) show the corresponding dQ/dV-plots obtained from the potential profiles for the first three cycles by differentiating the capacity $Q$ with respect to the voltage $V$. (Electrolyte: 1 M $NaClO_4$ in EC/PC (1:1), 20 mA $g^{-1}$). The full data set of 200 cycles (cycle 1 to 5: 20 mA $g^{-1}$, cycle 6 to 10: 50 mA $g^{-1}$, cycle 11 to 15: 100 mA $g^{-1}$, cycle 16 to 20: 200 mA $g^{-1}$, cycle 21 to 200: 50 mA $g^{-1}$) can be found in Figure SI 4.

seen from the XRD-signal after 100 cycles (blue). Moreover, a new peak appears at 16.44° after 100 cycles.

Figure 5b shows the development of the coulombic efficiency, i.e. the charge storage efficiency, upon continuous cycling. During the first few cycles, the µm-sized samples have slightly higher coulombic efficiencies compared to the nanomaterials. At prolonged cycling, a decrease is observed for the micromaterials, while the coulombic efficiency of the nanomaterials and especially the sonicated $V_2O_5$ remains constant. All materials have a coulombic efficiency higher than 98% after 200 cycles, with the exception of the $TiO_2$ blended $V_2O_5$ nanobundles, which show a 96% coulombic efficiency.

Besides the electrode capacity, one must also consider the electrode potential in order to evaluate the electrode performance. Integrating the potential-profiles in Figure 4 and Figure SI 5 yields the energy density of the electrode (in combination with a Na metal negative electrode with negligible overpotential) as a function of cycle number (Figure 5c). Again, one can note that the sonicated $V_2O_5$ nanobundles perform best with respect to energy density in comparison to the other materials. During the first cycles, the pure $V_2O_5$ nanobundles have an energy density (charge) of well above 500 mWh $g^{-1}$, which, however, quickly fades. After 200 cycles, an energy density of 248 mWh $g^{-1}$ remains. Thus, for practical application, the energy density is a more meaningful parameter than the electrode capacity.

Figure 5d shows the energy efficiency of each material as a function of cycle number. The energy efficiency measures how efficiently electric energy can be stored in the electrode and also includes energy losses. Here, a huge gap in performance between the nanomaterials and the micromaterials can be observed: the quickly fading energy efficiency of the solvothermal $V_2O_5$ hollow micro particles is below 60% after 200 cycles, whereas the energy efficiency of the sonicated $V_2O_5$ nanobundles fades less and is close to 80%. This plot also illustrates the advantage of the nanomaterials at higher rates, since almost no efficiency change at higher rates is observed for the nanomaterials, while a large decrease is observed for the commercial and the solvothermal samples, especially at 200 mA $g^{-1}$.

Figure SI 9 shows the average operating potential of each electrode material. Since electric energy is defined as the product of voltage and electric charge, the operating potential $V$ (with respect to $Na/Na^+$) can be determined from the ratio of the energy density $E$ and the specific capacity $Q$: $V = E/Q$. This way, one obtains a measure for the average operating potential for both, charge (open symbols in Figure SI 9) and discharge (solid symbols in Figure SI 9). Generally, one sees that the nanomaterials operate at more positive potential than the micromaterials, both when charging and discharging them. The increased discharge potential of the nanomaterials is beneficial to reach high power densities when consuming the electric charge in an electric device. The slight potential jiggles noticeable are caused by a fluctuating room temperature in the lab and have the rhythm of one day. The potential difference between charge and discharge is also reflected in the energy efficiency of each material shown in Figure 5d. Figure SI 10 plots the potential difference between charge and discharge as a function of cycle number. It is obvious that the

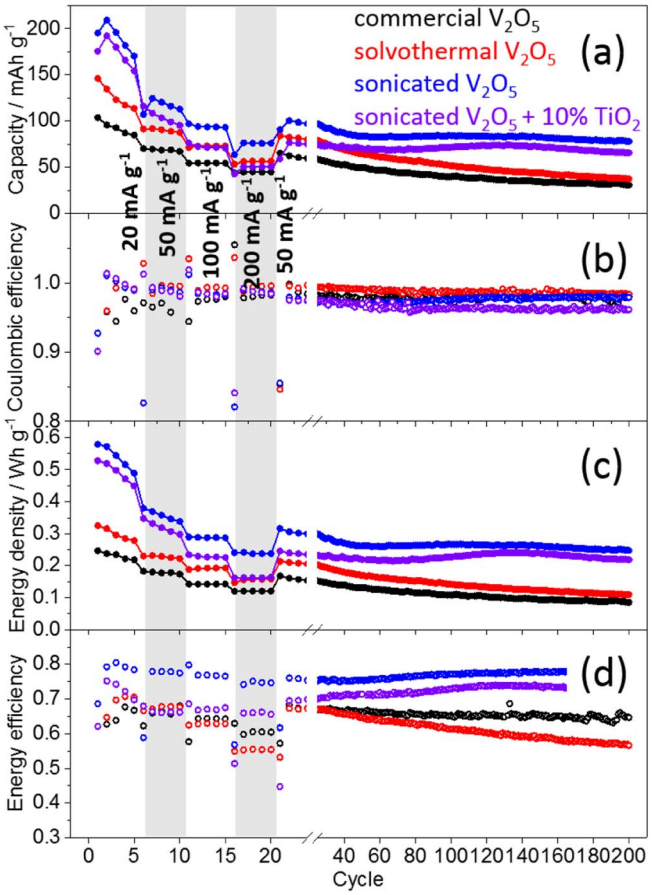


**Figure 5.** Comparison of (a) the electrode capacities upon charging, (b) the coulombic efficiencies, (c) charging energy densities as well as (d) the energy efficiencies of the different samples as a function of cycle number.

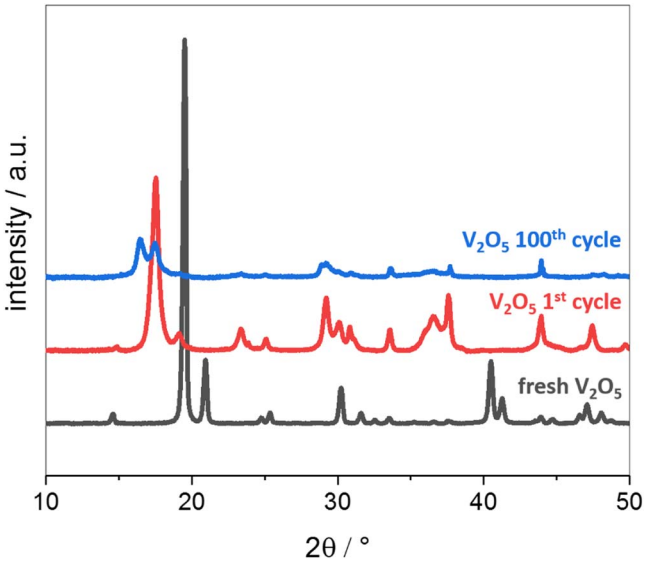


**Figure 6.** Effect of charge/discharge cycles on the XRD pattern of a micro-granular $V_2O_5$ electrode in a NIB with the uncycled $V_2O_5$ electrode (gray), the $V_2O_5$ electrode after 1 cycle (red) and after 100 cycles (blue). The electrodes were in charged state (de-sodiated) for XRD measurements.

potential losses are smallest for the sonicated $V_2O_5$ nanobundles. Additionally, Figure SI 9 and Figure SI 10 clearly demonstrate that the potential losses at high rates are smaller for the nanomaterials.

Table I summarizes the core findings of the charge-/discharge-tests of the different materials synthesized. The second and third columns show the discharge capacity of the first and second cycle, respectively. In case of the commercial $V_2O_5$ this includes the irreversible insertion of the first Na-ion into the $V_2O_5$ lattice, which results in an irreversible loss of capacity in the first cycle (fourth column). It is interesting to note that the two nanomaterials, i.e. the sonicated $V_2O_5$ nanobundles and the $TiO_2$ blended $V_2O_5$ nanobundles, have a significantly lower discharge capacity of the first cycle and the capacity after the first cycle even increases. The coulombic efficiency in the fifth column is given as a measure of how efficiently charge is stored in the electrode. Since during initial cycling this value can vary, the coulombic efficiency of the 100$^{th}$ cycle is shown here. Here, the nanomaterials have a lower coulombic efficiency compared to the two micromaterials. Moreover, the capacity loss per cycle is shown in the sixth column, indicating the lifetime of the electrode material, which is best for the $TiO_2$ blended $V_2O_5$ nanobundles. Besides this, the energy density and the corresponding energy efficiency after 100 cycles are shown. The last parameter shown in this table is the discharge potential of the 100$^{th}$ cycle.

In order to further understand the influence of the electrode morphology on the battery performance and to analyze the (pseudo-) capacitive contribution to the electrode capacity, a scan rate variation in a CV-study as described by Wang et al.[42] was done (Figure SI 11a). CVs of well cycled (20 cycles) electrodes of commercial $V_2O_5$ and sonicated $V_2O_5$ were measured at different potential sweep rates. From the slope of the *log(i)* vs. *log(ν)* plot (Figure SI 11b), one can extract the exponent (*b*-value) of the potential sweep rate *ν*, which equals 1 for a purely capacitive current ( $i_{capacitive} = k_1\ \nu^{b=1}$) and 0.5 for a purely diffusion controlled current ( $i_{intercalation} = k_2\ \nu^{b=0.5}$). This approach can provide information about the relative contributions of surface controlled (pseudo-) capacitive currents and actual intercalation currents even though it is only approximately valid, as for quasi-reversible reactions and in the presence of a finite diffusion length also the faradaic current connected with bulk diffusion will not be proportional to $\nu^{0.5}$. A plot of the obtained *b*-values as a function of electrode potential is shown in Figure SI 11c for the commercial $V_2O_5$ microparticles and the sonicated $V_2O_5$ nanobundles. One sees that the *b*-value of the nanosized material is close to 1 in the entire potential range, which indicates a dominant contribution of capacitive currents. The micrometer sized material on the other hand also shows a dominant contribution caused by an intercalation reaction in the potential range between ca. 2.7 V and 2.0 V.

A further analysis of this study is presented in Figure SI 12a, where an exemplary plot of $i\nu^{-1/2}$ *vs.* $\nu^{1/2}$ is shown. Extracting the slope and the intercept of the plot from a linear fit, one obtains the values $k_1$ and $k_2$, which allows the calculation of the capacitive and the intercalation current. Figure 7 shows the outcome of this analysis and compares the capacitive contribution for the commercial $V_2O_5$ microparticles (a) and the sonicated $V_2O_5$ nanobundles (b). One can see that the major contribution for the amorphous sonicated $V_2O_5$ nanoparticles can be attributed to (pseudo-) capacitive currents. The crystalline commercial $V_2O_5$ microparticles on the other hand also have a significant contribution caused by bulk $Na^+$-intercalation in the range between ca. 2.7 V and 2.0 V. Figure SI 12b illustrates the strength of Wang´s et al. method.[42] Here, the capacitive as well as the intercalation contribution are separately shown. The sum of both currents (green), which are extracted from the fit parameters of the $i\nu^{-1/2}$ *vs.* $\nu^{1/2}$ plots, fits very well to the measured CV.

## Discussion

Figure 2 systematically studies the potential induced phase transitions with $V_2O_5$ as the cathode material in a NIB. Upon discharge to 1.5 V, a phase transition from the pristine orthorhombic α-$V_2O_5$ (*Pmmn* space group)[36] to the sodiated α'-$NaV_2O_5$ phase (*Pmmn* space group)[36] is observed. According to the inserted electric charge, the

**Table I. Summary of the battery performances of the different $V_2O_5$ electrodes in comparison, including the capacity of the first and second discharge, the irreversible capacity loss after the first cycle, the coulombic efficiency of the 100th cycle, the capacity loss per cycle, the energy density of the 100th cycle, the energy efficiency of the 100th cycle and the discharge voltage after 100 cycles.**

| $V_2O_5$ sample | Capacity 1st discharge / mAh $g^{-1}$ | Capacity 2nd discharge / mAh $g^{-1}$ | Capacity loss 1st cycle / mAh $g^{-1}$ | Coulombic efficiency 100th /% | Capacity loss per cycle / mAh $g^{-1}$ | Energy density 100th / mWh $g^{-1}$ | Energy efficiency 100th /% | Discharge voltage vs $Na/Na^+$ 100th / V |
|---|---|---|---|---|---|---|---|---|
| commercial | 234.6 | 91.9 | 142.7 | 98.1 | 0.192 | 108.4 | 65.3 | 1.81 |
| solvothermal | 303.6 | 129.4 | 174.2 | 98.7 | 0.259 | 141.5 | 61.4 | 1.70 |
| sonicated | 195.3 | 209.2 | −13.9 | 97.6 | 0.124 | 266.5 | 77.2 | 2.38 |
| sonicated + $TiO_2$-blended | 175.7 | 192.3 | −16.6 | 96.5 | 0.061 | 227.2 | 72.9 | 2.23 |

following irreversible reaction is proposed:

$$V_2O_5 + Na^+ + e^- \rightarrow NaV_2O_5 \quad [1]$$

During this phase transition the interlayer distance of the orthorhombic $V_2O_5$ lattice increases from 4.55 Å to 5.05 Å as a result of the $Na^+$-intercalation (Figure 3). The fact that the (*hkl*)-peaks with a non-zero *l*-value shift to lower angle while the (*hk0*)-peaks remain unaffected during sodiation suggests that the Na-ions are solely inserted into the interlayer spacing of the orthorhombic $V_2O_5$ lattice.

Being further discharged to 1.0 V, a second Na-ion is, however, reversibly inserted into the α'-$NaV_2O_5$ electrode without a phase transition of the $NaV_2O_5$ lattice (XRD) according to:

$$NaV_2O_5 + Na^+ + e^- \rightleftharpoons Na_2V_2O_5 \quad [2]$$

The formed $Na_2V_2O_5$ corresponds to a theoretical capacity of 235.2 mAh $g^{-1}$, which is almost reached in the first discharge of the commercial $V_2O_5$ electrode (Table I, Figure 4a). Thus, in a NIB it is not the α-$V_2O_5$, which is reversibly cycled, but rather the α'-$NaV_2O_5$ phase. Hence, the actual cathode material should not be called $V_2O_5$-, but $NaV_2O_5$-cathode instead.

Performing a deep discharge down to 0.01 V, the CV in Figure 2c shows a further phase transition, where the determination of the stoichiometry from the CV peak suggests the uptake of a third Na-ion:

$$Na_2V_2O_5 + Na^+ + e^- \rightarrow Na_3V_2O_5 \quad [3]$$

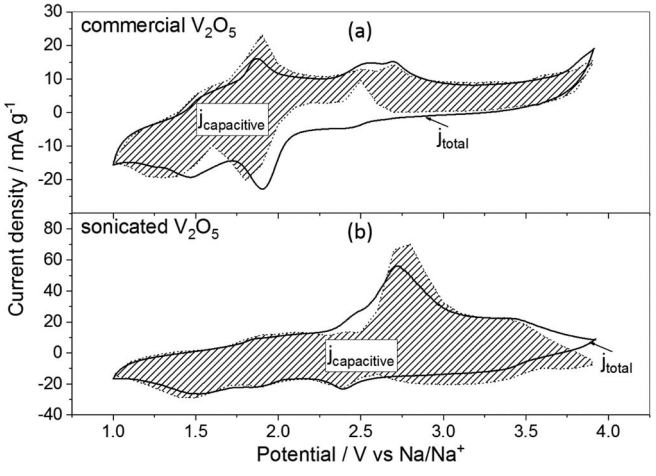


**Figure 7.** Comparative study of the (pseudo-) capacitive contribution to the electrochemical current in dependence of the $V_2O_5$ electrode morphology ((a) commercial $V_2O_5$, (b) sonicated $V_2O_5$). The solid line is a CV measured at 100 μV $s^{-1}$, whereas the dashed line depicts the current reconstructed from the linear relation of current density and potential sweep rate for capacitive currents.[42] Prior to the scan rate variation, the electrodes were charged/discharge between 4 V and 1 V at 100 mA $g^{-1}$ for 20 cycles in order to stabilize them. Afterwards, the CVs were measured at 100 μV $s^{-1}$, 80 μV $s^{-1}$, 60 μV $s^{-1}$ and 40 μV $s^{-1}$.

The difference between the experimentally observed $Na_{2.6}V_2O_5$ and the suggested stoichiometry of $Na_3V_2O_5$ is caused by the fact that the charge was determined from the CV peaks, while in the two previous cases it was determined from the potential profile of the first discharge curve (Figure 4a), which usually is the more accurate method. The $Na_3V_2O_5$ composition was also found by Moretti et al.,[29] who used a $V_2O_5$-aerogel as anode material. The observed phase transition only occurs in the first discharge. Thus, the insertion of a third Na-ion results in an irreversible crystal structure transformation, in which the long-range order of the host structure is destroyed, resulting thereafter in smooth and featureless charge/discharge curves as observed in Moretti´s et al. study.[29,38] This loss of long range order in the crystal lattice is also confirmed by XRD-measurements (Figure 3). Some Na-ions can still be stored in the electrode in the consecutive cycles, as can be seen from the current difference between negative and positive sweep, but not to an extent of practical relevance for a battery operation.

The found phase transitions therefore suggest that, when operated as cathode, $NaV_2O_5$ must be cycled above 1.0 V. Taking a look at the second and third cycle in Figure 2b, one sees that the peaks become blurred with time, which can also be seen in the potential profiles of the charge/discharge curves becoming smoother and showing less features (Figure 4a). Again, the loss of peaks in the CVs, respectively the loss of plateaus in the charge/discharge curves can be a result of a loss of the long-range order of the α'-$NaV_2O_5$ crystals upon continuous sodiation/de-sodiation.[38,43] This effect is confirmed by the decrease of the XRD-peak intensities with prolonged cycling (Figure 6) and is expected to be more severe for materials consisting of large, μm-sized crystallites, than for nanomaterials, since nanomaterials per se do not possess a long-range crystalline order.

Knowing about the fundamental phase transitions related to the insertion of Na-ions into the $V_2O_5$-host, the influence of electrode morphology on the battery performance can be discussed. With the exception of the V-(IV)-oxide XPS signal for the solvothermal hollow $V_2O_5$ microspheres, the synthesized electrode morphologies show the typical $V_2O_5$ XPS signals and XRD peaks for all samples (Figure SI 1 and Figure SI 2). The intensity ratio of crystalline to amorphous XRD signal allows to estimate the crystallinity of the materials, which has an effect on the shape of the charge/discharge curves: the less crystalline the sample, the less pronounced plateaus are in the charge/discharge curves, which results in the smaller peaks in the respective dQ/dV-plots (Figure 4). Thus, the loss of plateaus upon continuous sodiation/de-sodiation according to XRD (Figure 6) is caused by a loss of crystalline order. In literature similar effects are described, where the insertion of bigger ions, such as $Na^+$ and $K^+$ lead to an amorphization of the vanadium-oxide lattice.[44] Disassembling the batteries after cycling shows a greenish discoloration of the glass fiber separators, which is another strong indication for a loss of active material from the electrode, probably as a result of the amorphization and the loss of structural integrity due to a crumbling of the $V_2O_5$ particles.

The capacities of the nanostructured materials (Figure 5) are larger than those for the commercial $V_2O_5$ microparticles and the hollow microspheres, and the irreversible capacity loss of micromaterials during first discharge is not observed for the former. Instead, the

nanomaterials retain their original capacity, meaning that the intercalation mechanism of the highly crystalline materials, as discussed in Equations 1 to 3 is different. This is caused by the prevalence of surface controlled processes, as confirmed by the (pseudo-) capacitive behavior. Figure 7 proofs the (pseudo-) capacitive character of the nanomaterial, probably mainly due to an adsorption capacity, compared to the intercalation dominated micromaterial. This might be an effect of the increased degree of amorphization and due to enlarged surface area.

Besides the increased capacity, the average working potential of the nanomaterials is also increased by ca. 0.5 V, which can be seen from the dQ/dV-plots in Figure SI 6 and from Figure SI 7. Also when taking a close look at the dQ/dV-plots of the first three cycles of the 'highly' crystalline samples (commercial $V_2O_5$ and hollow $V_2O_5$ microspheres in Figures 4e and 4f, respectively), one realizes that the peaks shift to slightly more positive potentials each cycle, which again might be related to an ongoing amorphization when the $V_2O_5$ particles break up upon sodiation/de-sodiation. Thus, one can assume that amorphous materials may offer a more positive intercalation/de-intercalation potential for the Na-ions. Several factors can contribute to the observed differences: Due to the decreased diffusion length in the host particles, one would expect an enhanced $Na^+$-diffusion. While this could enhance the kinetics and increase the rate capability of the intercalation/de-intercalation reactions, it should, however, not affect the energy levels of the reaction. Another reason could be the increased number of surface defects of the amorphous material, offering more and energetically different intercalation sites to the Na-ions. Moreover, due to the nanostructure the intercalation positions of the Na-ions in the electrode all are 'near surface', and the larger amorphous content will introduce defects and consequently result in deviations from the ideal crystalline lattice structure. Both contributions may facilitate the sodium insertion and therefore may increase the intercalation-/de-intercalation-potential. This is confirmed by the (pseudo-) capacitive behavior of the sonochemically prepared nanomaterials.

At increased rates, all materials show a capacity decrease and an increase of the potential difference between oxidation and reduction. This behavior is influenced by the charge transfer resistance, the electronic resistance of the electrode layer and the diffusion of Na ions within the active material. Since the electrolyte is the same in all cases, it should not influence the different capacity responses of the materials at higher rates. The main difference between the positive electrodes for the different materials is the morphology and the concomitant diffusion length for the Na-ions inside the active material. Na-ions have to diffuse through the bulk of the electroactive material, and this can limit the applicable charge/discharge rates. Thus, due to the increased surface-to-bulk ratio of the nanomaterials, the diffusion limitation is not as severe as for the micromaterials. Moreover, (pseudo-) capacitive charging is not diffusion limited, resulting in higher accessible current rates. In addition, the different particle morphology can influence the electrode layer structure and the contact to the carbon particles providing electron conduction. For smaller particles, a reduced limitation due to the electron transport within the vanadium oxide lattice can be expected, and thus a lower resistance of the electrode layer, favoring improved rate capability and lower potential differences between reduction and oxidation. Similar observations were also made for other electrode materials with poor electronic conductivity, for example for polyanionic compounds such as $Na_3V_2(PO_4)_3$, where nano-structuring increased the contact to the conductive carbon, being an effective strategy to tackle the low electronic conductivity.[9,45]

Compared to the micromaterials, the lifetime of the nanomaterials is prolonged. As already discussed above, the loss in capacity results from an amorphization of the $V_2O_5$ particles (Figure 6) and a loss of electric contact, which results in the capacity fading but occurs to a lesser extent for the nanomaterials.

$V_2O_5$ electrodes used as Li-host in LIBs suffer from similar problems. A common strategy to tackle the stability issue is to mix small amounts of $TiO_2$ to the $V_2O_5$, which enhances the battery lifetime.[30,33,46–49] Different stabilizing mechanisms are debated in literature. One protective mechanism suggested by Davies et al.[33] is based on the preferential $Ti^{4+}$-reduction compared to the $V^{5+}$-reduction, preventing the reorganization of the microstructure of this material. Another mechanism is ascribed to changes in the lattice structure and interaction force between two adjacent $V_2O_5$ layers when adding $TiO_2$.[46] A third possibility of capacity fading is attributed to a detachment/dissolution of $V_2O_5$ into the electrolyte, which can be suppressed by embedding the $V_2O_5$ into a $TiO_2$ matrix.[30,48] In our study, the effect of stabilizing the $V_2O_5$ electrode with $TiO_2$ against degradation upon cycling was transferred to a NIB. The XRD data of this material (Figure SI 1) only shows very weak peaks, probably caused by the strong amorphization. The O1s XPS-peak of pure $TiO_2$ typically is in the range from 529.4 eV to 531.2 eV,[50] which is close to the 531.3 eV found here. Thus, neither the XRD nor the XPS data suggest an integration of the $TiO_2$ into the $V_2O_5$ lattice, but rather a homogenous mixture of both, which is why the stabilizing mechanism via a stabilized lattice structure between two adjacent $V_2O_5$ layers does not seem plausible for this work.

In the present case, the $TiO_2$-blended electrode shows the least performance degradation of all materials (Figure 5 and Table I), however, it does not seem to be significantly better than the pure $V_2O_5$ nanobundles. This in turn means that an amorphization of the $V_2O_5$ crystals indeed is a plausible degradation mechanism for the microcrystalline samples, since the initially 'amorphous' nanomaterials degrade much less than the higher crystalline commercial $V_2O_5$ and the hollow $V_2O_5$ microspheres because they already are amorphous from the beginning. This phenomenon is also described by Uchaker et al.[27] Consequently, amorphous $V_2O_5$ is advantageous compared to highly crystalline $V_2O_5$ in terms of cycling stability, probably due to better accommodation of volume changes, and a reduced loss of electric contact of active material to the electrode, the carbon black and current collector.

Another remarkable observation is the fact that in spite of a small performance degradation of this material the coulombic efficiency is the lowest. Low coulombic efficiencies are an indication for side reactions, such as the formation of a solid electrolyte interphase (SEI). The larger surface area of the nanomaterials and the addition of the $TiO_2$ due to the catalytic properties of titania for the electrochemical oxidation of organic solvents might both enhance the electrolyte decomposition and result in lower coulombic efficiencies.[51]

Moreover, the capacity and energy density losses of the $TiO_2$-blended sample compared to the pure $V_2O_5$ nanobundles is lowered by 12 to 16%. This suggests that the $TiO_2$, which has a 10% mass contribution to the electrode material, is not electrochemically active and consequently only lowers the specific electrode capacity and energy density accordingly.

At last, the suitability of the tested materials for practical application (e.g. in a full cell) shall be discussed. In earlier work, we conducted studies on graphite negative electrodes in NIBs and on the formation of a solid electrolyte interphase.[52,53] The only material possessing somewhat suitable properties for battery application is the pure nanostructured $V_2O_5$ nanobundles, outperforming all other materials with a practical capacity (100$^{th}$ cycle) of 85 mAh $g^{-1}$, a coulombic efficiency of around 98%, a practical energy density of 266.5 mWh $g^{-1}$, an energy efficiency of 77.2% and a discharge voltage of 2.4 V. Compared to other positive electrode materials for NIBs, such as other transition metal oxides, hexacyanometallates, polyanionic compounds and organic electrodes, the $V_2O_5$ electrodes have slightly lower capacities and voltages as well as large voltage losses between charge and discharge, resulting in rather poor energy efficiencies.[9,54] An actual application of these materials therefore would require further improvements in capacity and operation voltage that might be realized by further nano-structuring, which may also reduce the energy losses.

## Conclusions

The phase transitions of the $Na_xV_2O_5$ system were studied by CV and XRD, which revealed that the first $Na^+$ irreversibly intercalates

into the α-phase $V_2O_5$ above 1.5 V, yielding the α'-$NaV_2O_5$. During this phase transition, the Na-ions intercalate into the interlayer spacing of the orthorhombic $V_2O_5$ lattice, which results in a lattice expansion from 4.55 Å to 5.05 Å. Between 1.5 V and 1.0 V, a second $Na^+$ reversibly intercalates without phase transition, while the insertion of a third $Na^+$ at even lower potential results in an irreversible phase transition. Based on these findings, different $V_2O_5$-morphologies were synthesized, including hollow $V_2O_5$ microspheres, $V_2O_5$ nanobundles and $V_2O_5$ nanobundles blended with 10% $TiO_2$. Those materials were compared to commercially available $V_2O_5$ and all showed an improved battery performance. The sonochemically prepared $V_2O_5$ nanomaterials, however, showed by far the best performance with a practical capacity of 85 mAh $g^{-1}$, an operation potential of ca. 2.4 V, an energy density of 266.5 mWh $kg^{-1}$ and a capacity retention of 83% after 100 cycles.

The key parameter determining the battery performance of a $NaV_2O_5$ electrode seems to be the degree of its amorphization. Upon continuous sodiation/de-sodiation the $NaV_2O_5$ electrode degrades, which results in a capacity loss. Materials, which are amorphous prior to cycling in a NIB, and consist of nanoparticles, show much less capacity fading, since they can hardly become more amorphous and possibly detached material does not lose electric contact to the electrode. Thus, a high grade of amorphization seems beneficial in terms of electrode lifetime. Additionally, the amorphous nanomaterials show an increased capacity for fast charging/discharging due to the decreased diffusion length for the Na-ions in the crystal lattice, the increased (pseudo-) capacitive capacity contribution and a better electric contact to the conductive carbon. The nanomaterials also can be operated at an approximately 0.6 V increased potential, since Na-intercalation occurs at energetically different, 'near surface' intercalation sites.

In addition to the morphology effect on the battery performance, another strategy to prolong the cycle life was pursued by blending the $V_2O_5$ nanobundles with $TiO_2$. The well-known stabilizing effect of $TiO_2$ in the Na intercalation behavior of $V_2O_5$ was also observed in this study, however, the effect was not strong enough to rectify the loss in capacity and electrode potential of the pure nanomaterial. The better way to stabilize $V_2O_5$ electrodes upon continuous sodiation/de-sodiation is to increase the degree of amorphization of the active material prior to the electrode preparation.

In conclusion, one can say that nanostructured $V_2O_5$ is a potential candidate as a positive electrode material for future NIB applications if capacities and voltages can be increased by further reducing the $V_2O_5$ nano-size, which also increases the energy efficiency and lifetime of the battery. The nano-structuring itself and a combination with other methods to increase the electric conductivity, like increasing the content of conductive carbon might still bury a lot of optimization potential.

## Acknowledgment

This work was funded by the German Ministry of Education and Research (BMBF) within the Sino-German Network on Electromobility (reference no. 16N11930) and the IAPS project (reference no. 01DO12001), which is gratefully acknowledged. The authors appreciate financial support from the National Key Project on Basic Research (2016YFB0901703) and the Natural Science Foundation of China (U1664256). This work was also supported by the State Key Fundamental Research 973 Program of China (2015CB251104) and the US-China Clean Energy Research Center-Clean Vehicle Consortium (CERC-CVC). The CERC-CVC in China is supported by the MOST (Ministry of Science and Technology) of China (2016YFE0102200). The support of Prof. Heiz (Chemistry Department, Technische Universität München), Prof. Gasteiger (Chemistry Department, Technische Universität München), and Prof. Knoll (Institute of Informatics VI, Technische Universität München) and the use of their facilities are appreciated. The support by EPSRC through NECEM (EP/R021503/1) and by Newcastle University is gratefully acknowledged.

## ORCID

Lukas Seidl https://orcid.org/0000-0002-8747-115X
Oliver Schneider https://orcid.org/0000-0003-1158-6169

## References

1. S. W. Kim, D. H. Seo, X. Ma, G. Ceder, and K. Kang, *Adv. Energy Mater.*, **2**, 710 (2012).
2. B. L. Ellis and L. F. Nazar, *Curr. Opin. Solid State Mater. Sci.*, **16**, 168 (2012).
3. M. D. Slater, D. Kim, E. Lee, and C. S. Johnson, *Adv. Funct. Mater.*, **23**, 947 (2013).
4. K. Kubota, N. Yabuuchi, H. Yoshida, M. Dahbi, and S. Komaba, *MRS Bull.*, **39**, 416 (2014).
5. N. Yabuuchi, K. Kubota, M. Dahbi, and S. Komaba, *Chem. Rev.*, **114**, 11636 (2014).
6. D. Kundu, E. Talaie, V. Duffort, and L. F. Nazar, *Angew. Chemie - Int. Ed.*, **54**, 3432 (2015).
7. M. H. Han, E. Gonzalo, G. Singh, and T. Rojo, *Energy Environ. Sci.*, **8**, 81 (2015).
8. H. Pan, Y.-S. Hu, and L. Chen, *Energy Environ. Sci.*, **6**, 2338 (2013).
9. X. Xiang, K. Zhang, and J. Chen, *Adv. Mater.*, **27**, 5343 (2015).
10. D. W. Su, S. X. Dou, and G. X. Wang, *J. Mater. Chem. A*, **2**, 11185 (2014).
11. X. Xu et al., *Nano Lett.*, **15**, 3879 (2015).
12. W. Wan and H. Wang, *Int. J. Electrochem. Sci.*, **10**, 3177 (2015).
13. S. P. Ong et al., *Energy Environ. Sci.*, **4**, 3680 (2011).
14. F. Klein, B. Jache, A. Bhide, and P. Adelhelm, *Phys. Chem. Chem. Phys.*, **15**, 15876 (2013).
15. Y. Cao et al., *Nano Lett.*, **12**, 3783 (2012).
16. J. M. Tarascon and M. Armand, *Nature*, **414**, 359 (2001).
17. S. Wang et al., *J. Mater. Chem.*, **21**, 6365 (2011).
18. A. M. Cao, J. S. Hu, H. P. Liang, and L. J. Wan, *Angew. Chemie - Int. Ed.*, **44**, 4391 (2005).
19. J. Liu, Y. Zhou, J. Wang, Y. Pan, and D. Xue, *Chem. Commun.*, **47**, 10380 (2011).
20. A. Pan, H. Bin Wu, L. Yu, T. Zhu, and X. W. Lou, *ACS Appl. Mater. Interfaces*, **4**, 3874 (2012).
21. K. Zhu et al., *ChemElectroChem*, **2**, 1660 (2015).
22. A. Moretti, F. Maroni, I. Osada, F. Nobili, and S. Passerini, *ChemElectroChem*, **2**, 529 (2015).
23. C. Niu et al., *Electrochim. Acta*, **182**, 621 (2015).
24. X. Rui et al., *Nanoscale*, **5**, 556 (2013).
25. S. Tepavcevic et al., *ACS Nano*, **6**, 530 (2012).
26. D. Su and G. Wang, *ACS Nano*, **7**, 11218 (2013).
27. E. Uchaker et al., *J. Mater. Chem. A*, **2**, 18208 (2014).
28. Q. Wei et al., *J. Mater. Chem. A*, **3**, 8070 (2015).
29. A. Moretti et al., *J. Electrochem. Soc.*, **162**, A2723 (2015).
30. S. Tian, A. Xing, H. Tang, Z. Bao, and G. Wu, *J. Mater. Chem. A*, **2**, 2896 (2014).
31. X. Zhou, T. He, X. Chen, L. Sun, and Z. Liu, *RSC Adv.*, **6**, 53925 (2016).
32. M. Xie et al., *J. Mater. Chem. A*, **4**, 537 (2016).
33. A. Davies, R. J. Hobson, M. J. Hudson, W. J. Macklin, and R. J. Neat, *J. Mater. Chem.*, **6**, 49 (1996).
34. A. Byström, K.-A. Wilhelmi, and O. Brotzen, *Acta Chem. Scand.*, **4**, 1119 (1950).
35. C. Delmas, H. Cognac-Auradou, J. Cocciantelli, M. Ménétrier, and J. Doumerc, *Solid State Ionics*, **69**, 257 (1994).
36. R. Haberkorn, J. Bauer, and G. Kickelbick, *Zeitschrift für Anorg. und Allg. Chemie*, **640**, 3197 (2014).
37. J.-M. Savariault, J.-L. Parize, D. Ballivet-Tkatchenko, and J. Galy, *J. Solid State Chem.*, **6**, 1 (1996).
38. K. West, B. Zachau-Christiansen, T. Jacobsen, and S. Skaarup, *Solid State Ionics*, **28–30**, 1128 (1988).
39. E. Uchaker, N. Zhou, Y. Li, and G. Cao, *J. Phys. Chem. C*, **117**, 1621 (2013).
40. C.-J. Mao, H.-C. Pan, X.-C. Wu, J.-J. Zhu, and H.-Y. Chen, *J. Phys. Chem. B*, **110**, 14709 (2006).
41. J. H. Bang and K. S. Suslick, *Adv. Mater.*, **22**, 1039 (2010).
42. J. Wang, J. Polleux, J. Lim, and B. Dunn, *J. Phys. Chem. C*, **111**, 14925 (2007).
43. V. Augustyn and B. Dunn, *Electrochim. Acta*, **88**, 530 (2013).
44. S. Hartung et al., *Adv. Energy Mater.*, **6**, 1 (2016).
45. Q. Wang, B. Zaho, S. Zhang, X. Gao, and C. Deng, *J. Mater. Chem. A*, **3**, 7732 (2015).
46. Y. Wang, K. Takahashi, K. H. Lee, and G. Z. Cao, *Adv. Funct. Mater.*, **16**, 1133 (2006).
47. M. J. Armstrong et al., *J. Mater. Chem. A*, **1**, 12568 (2013).
48. X. Zhou, T. He, X. Chen, L. Sun, and Z. Liu, *RSC Adv.*, **6**, 53925 (2016).
49. M. Xie et al., *J. Mater. Chem. A*, **4**, 537 (2016).
50. A. V. Naumkin, A. Kraut-Vass, S. W. Gaarenstroom, and C. J. Powell, *NIST X-ray Photoelectron Spectrosc. Database*, March 2017 (2017).
51. C. Rüdiger et al., *ChemCatChem*, **5**, 3219 (2013).
52. L. Seidl, S. Martens, J. Ma, U. Stimming, and O. Schneider, *Nanoscale*, **8**, 14004 (2016).
53. L. Seidl et al., *Energy Environ. Sci.*, **10**, 1631 (2017).
54. H. Kim et al., *Adv. Energy Mater.*, **6** (2016).